Electronic Supplementary Material (ESI) for Nanoscale Advances.

Supporting information

Biohybrid materials comprising an artificial peroxidase and differently shaped gold nanoparticles

Emilia Renzi,[a,‡] Alessandra Esposito,[a,‡] Linda Leone,[a] Miriam Chávez,[b] Teresa Pineda,[b] Angela Lombardi*[a] and Flavia Nastri*[a]

Affiliation

[a]Department of Chemical Sciences, University of Naples Federico II, Complesso Universitario Monte S. Angelo, via Cintia, Naples, 80126, Italy

[b]Department of Physical Chemistry and Applied Thermodynamics, Institute of Chemistry for Energy and Environment, University of Cordoba, Campus Rabanales, Ed. Marie Curie, Córdoba, E-14014, Spain

Table of contents

S1 | | Materials and instrumentation

Solvents with a high degree of purity (Ups grade) were used in the preparation of solutions for UV-Vis and UV-Vis-NIR investigations and supplied by Romil (Cambridge, UK). $HAuCl_4$ solution (30% w/w), ascorbic acid (AA, 99%), cetyltrimethylammonium bromide (CTAB, 99%), lipoic acid (LA), silver nitrate ($AgNO_3$), sodium borohydride ($NaBH_4$), sodium polystyrene sulfonate (Na-PSS), sodium thiosulfate ($Na_2S_2O_3$), trisodium citrate (Na_3-citrate), potassium cyanide (KCN), H_2O_2 solution (30% *v/v*) and phosphate salts (monobasic and dibasic) were provided by Merck Life Science. All buffer solutions were prepared using water with a HPLC purity grade (Romil). Concentrated nitric and hydrochloric acids (UpA grade) were purchased from Romil (Cambridge, UK) and employed during the ICP-MS measurements. DBCO-$(PEG)_4$-NHS from Jena Bioscience was obtained from Applied Biosystem (Thermo Fisher Scientific, Waltham, MA, USA). UranyLess staining solution was purchased from Electron Microscopy Sciences (Hatfield, PA, USA). All reagents were used without further purification. Milli-Q water, produced using Milli-Q system (18.2 MΩ cm^{-1}) was purchased from Millipore (Sweden).

UV-Vis analysis and kinetic experiments were recorded using a Cary 60 spectrophotometer (Varian, Palo Alto, CA, USA), equipped with a thermostatic cell compartment, using quartz cuvettes with 0.1 cm, 0.01 cm and 1 cm path lengths. Wavelength scans were performed at 25 °C in the range 200-800 nm or 200-1000 nm, with a 600 nm min^{-1} scan speed. All data were blank subtracted.

UV-Vis-NIR spectra were acquired using a Jasco V-770 spectrophotometer (Easton, MD, USA.) equipped with a monochromator with automatically exchanged dual-grating, using quart cuvettes with 0.01 and 1 cm path lengths. Wavelength scans were performed at 25 °C in the range 200-1800 nm, with a 400 nm min^{-1} scan speed. All data were blank subtracted.

Bare and functionalized nanomaterials, as well as the prepared nanoconjugates, were purified by centrifugation cycles through Sigma Refrigerated Centrifuge 2K15 (B. Braun Biotech International; Melsungen, Germany) equipped with 12148-H or 12141-H rotors.

Circular Dichroism measurements were performed using a J-815 spectropolarimeter equipped with a thermostated cell holder (JASCO, Easton, MD, USA). CD spectra were collected using quartz cuvettes with 1 cm path lengths at 25 °C, from 260 to 200 nm with a 20 nm^{-1} scan speed. A quartz cell of 1 cm path length was used in all measurements.

A Thermo Fischer Scientific Nicolet 6700 FT-IR was employed to acquire the ATR spectra of the samples, using a ZnSe crystal, in absorbance mode with 4 cm^{-1} resolution. 128 scans were averaged for each spectrum in a range between 4000-500 cm^{-1}.

Transmission electron microscopy (TEM) images were obtained in bright field mode using a TEM TECNAI G^2 20ST, using copper grids covered by a carbon film (Agar Scientific Ltd., product S160, 200 mesh).

The gold content in the samples containing gold nanomaterials was evaluated through inductively-coupled plasma mass spectrometry (ICP-MS) measurements, performed with an Agilent 7700 ICP-MS instrument (Agilent Technologies) equipped with a frequency-matching radio frequency (RF) generator and 3rd generation Octapole Reaction System operating with helium gas. The following parameters were used: RF power: 1550 W, plasma gas flow: 14 L min^{-1}; carrier gas flow: 0.99 L min^{-1}; He gas flow: 4.3 mL min−1. ^{103}Rh was used as an internal standard (final concentration: 50 μg L^{-1}).

Malvern Zetasizer Nano ZS instrument was used to perform ζ-potential measurements at 25 °C with an applied voltage of 150 V. Disposable folded capillary cuvettes (DTS1070) were filled with the nanomaterial samples.

XPS analysis was performed with a MCD SPECS Phoibos 150 spectrometer (Servicio Central de Apoyo a la Investigación of the Universidad de Córdoba) by using non-monochromatized (12 kV, 300 W) Mg Ka radiation (1253.6 e V). The samples were mounted on a steel holder and transferred to the XPS analytical chamber, with a working pressure of less than $5 \cdot 10^{-9}$ Pa. The spectra were collected using a take-off angle of 45° with respect to the sample surface plane.

All molecular graphics pictures were generated with PyMOL software (DeLano Scientific Ltd), while chemical structures and reactions were drawn with ChemDraw Ultra 12. Data analysis was made with Origin Pro 9.0 software (Origin Lab Corporation, Northampton, MA, USA) and ImageJ software (National Institutes of Health, available free of charge at Web site rsb.info.nih.gov/ij/).

S2 | Route to the preparation of the nanoconjugates

S2.1 | CTAB-AuNRs

The method reported by Murphy *et al.*[1–3] and El-Sayed *et al.*[4] was followed. Seed solution: an aqueous CTAB solution (5.0 mL, 0.2 M) and a yellow aqueous solution of $HAuCl_4$ (5.0 mL, 0.5 mM) were mixed under stirring, to afford an orange solution.[5] Then, a freshly-prepared cold aqueous solution of $NaBH_4$ (0.6 mL, 0.01 M) was added under vigorous stirring (≈ 500 rpm) over 5 min at 25 °C. During the addition, a color change from orange to brown was observed, which was an indication of the formation of spherical seeds (≈ 5 nm). Growth solution: aqueous solutions of $AgNO_3$ (1.25mL, 4 mM) and CTAB (250.0 mL, 0.2 M) were mixed with a yellow aqueous solution of $HAuCl_4$ (250.0 mL, 1.0 mM) at 25 °C without stirring, which turned to orange.[6] Into this mixture, an aqueous solution of ascorbic acid (AA) (3.5 mL, 78.8 mM) was added, and the flask was hand-stirred until the solution became colorless due to Au^{3+}/Au^{+} reduction.[6] Afterwards, the seed solution (0.8 mL) was injected into a stirring (300 rpm) growth solution and the stirring was kept for half a min. A bluish-brown color slowly appeared within the first 20 min. Overall, the flask containing the whole mixture was kept for 16 h on a tilting plate at 29 °C, without magnetic stirring, to promote the gentle growth of rod-like nanostructures. After the synthesis, CTAB-AuNTs were promptly purified from the excess surfactant through 4 cycles of centrifugation (10000 rpm, 30 min, 25 °C) and resuspension in a freshly-prepared aqueous CTAB solution (2 mM).[7] After the first two cycles, the pellet was resuspended in a volume of CTAB solution (2 mM) equal to the initial volume of the colloidal solution, whereas the sample was concentrated up to 20 times after the last two cycles. The purified CTAB-AuNRs were stable at room temperature for several months.

S2.2 | CTAB-AuNTs

According to Pelaz *et al.*,[8] an aqueous solution of $HAuCl_4$ (25.0 mL, 2 mM) was mixed with a cold and freshly-prepared solution of $Na_2S_2O_3$ (30.0 mL, 0.5 mM). The color of the gold solution changed from pale yellow to brownish, due to the nucleation process and the formation of small AuNP seeds. For 9 min, the colloidal solution was stirred at room temperature. Additionally, an aqueous solution of $Na_2S_2O_3$ (5.0 mL, 0.5 mM) was injected into the seeds-containing solution, and a color change, from brownish to deep purple, was observed. This evidence has been related to the beginning of the growth of anisotropic gold nanotriangles. The reaction mixture was left undisturbed for 90 min, until no further changes in the absorption spectra were noticed. With this procedure, a colloid characterized by diversity in shape and size was obtained, including AuNTs of diverse sizes, along with differently-shaped gold nanomaterials (mostly nanoparticles). The purity

of the colloid was improved through size and shape purification by depletion flocculation, induced by the presence of the micellar surfactant CTAB. Briefly, aliquots of the colloidal mixture (2.0 mL) were put into falcon tubes and an aqueous solution of CTAB (1.44 mL, 0.4 M - final CTAB concentration was 0.167 M)[9] was added. The resulting solutions were kept undisturbed overnight for 12 h at a room temperature of ≈ 30 °C, to prevent CTAB crystallization. After that, a green-blue precipitate deposited on the bottom of the tube and was separated by a purple supernatant, containing most of the pseudo-spherical particles from the reaction crude. The supernatant was gently removed and the sedimented AuNTs were resuspended in Milli-Q water (300 μL), affording a concentrated solution of CTAB-AuNTs. Subsequently, CTAB concentration was decreased similarly to AuNRs, by performing four cycles of centrifugation (7000 rpm, 30 min, 25 °C) and resuspending the pellet in a freshly-prepared aqueous CTAB solution (2 mM).[7] The purified CTAB-AuNTs were kept in the dark at room temperature until further use and proved to be stable for several months.

S2.3 | PSS-AuNRs/AuNTs

PSS- and citrate-capped AuNRs and AuNTs were prepared following a procedure reported by Mehtala *et al.*,[10] with minor changes. Optical densities (O.D.) of AuNRs solutions were measured based on their plasmon resonance peak at extinction values below 1.0; O.D. values of concentrated samples were extrapolated after serial dilution. In stage 1, concentrated purified solutions of CTAB-AuNRs (2.0 mL) and CTAB-AuNTs (10.0 mL) were properly diluted with an aqueous solution of Na-PSS (MW_{av} = 70 kDa, final concentration 0.15% wt) to a final volume allowing to reach an O.D. = 0.5. The first incubation step was carried out for 2 h. Afterward, in stages 2 and 3, the mixtures containing AuNRs/AuNTs in presence of CTAB and Na-PSS were centrifuged (7000 rpm, 30 min, 25 °C for AuNRs, 6500 rpm, 15 min, 25 °C for AuNTs). Nearly 95% of the supernatant was decanted, and the retentate was redispersed in an aqueous solution of Na-PSS (0.15% wt, MW_{av} = 70 kDa) to a final volume equal to the initial one (16.0 ml) and allowed to interact for at least 1 h before the next step.

S2.4 | Citrate-AuNRs/AuNTs

In stage 4, the solutions of PSS-AuNRs/AuNTs (stage 3) were centrifuged (7000 rpm, 30 min, 25 °C for AuNRs, 6500 rpm, 15 min, 25 °C for AuNTs) and the pelleted nanomaterials were resuspended in an aqueous solution of Na_3-citrate (16.0 mL, 5 mM) and incubated for 12 h. In stage 5, the AuNRs/AuNTs containing colloidal solutions were subjected to the last centrifugation cycle

(7000 rpm, 30 min, 25 °C for AuNRs, 6500 rpm, 15 min, 25 °C for AuNTs) and the collected precipitates were finally redispersed in an aqueous solution of Na_3-citrate (16.0 mL, 5 mM). Citrate-stabilized AuNRs and AuNTs were stable for several months and were kept at 4 °C in the dark until further use.

S2.5 | Estimation of the AuNMs concentration

AuNMs concentration was estimated determining the gold concentration in each sample by ICP-MS analysis and assuming that all the gold is incorporated into the AuNMs with the density of the bulk gold (ρ_{gold} = 19 g cm^{-3}).[11] The volume of both AuNRs and AuNTs was determined, as reported in the literature,[12] on the basis of geometrical considerations as described in the following sections.

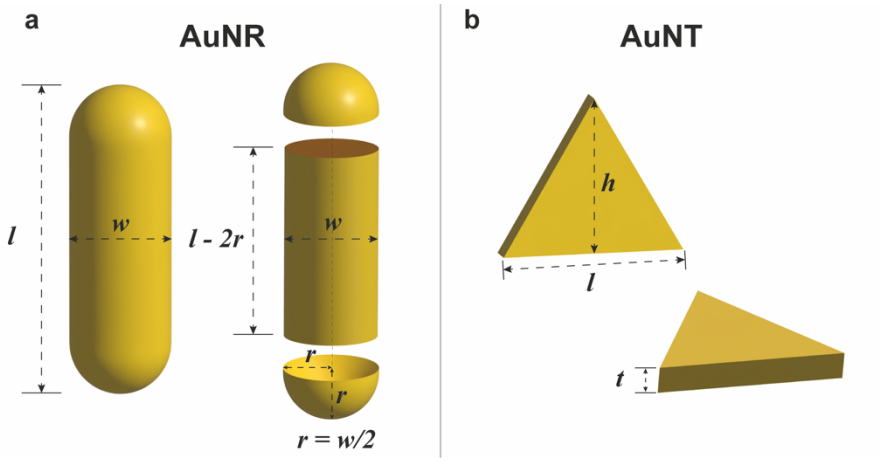

Figure S1. Geometry and shape of the gold nanomaterials. a) AuNR depicted as a cylinder with two hemispheres at each end, where the width (*w*) is defined by the radius of the rod (*r=w/2*) and the length (*l*). b) AuNT visualized as a triangular nanoprism with the edge length (*l*), height (*h*), and thickness (*t*).

- **AuNRs**

The shape of each AuNRs was treated as a cylinder capped with two hemispheres at both ends (Fig. S1a). The volume can be calculated by the following formula:

$$\boldsymbol{V_{AuNRs}} = \frac{1}{4}\pi w^2(l-w) + \frac{1}{6}\pi w^3 \qquad (\boldsymbol{Eq.\ S1})$$

where *l* is the average length of the rods and *w* is the width of AuNRs (evaluated from TEM analysis, see Table S1). AuNRs concentration can be derived from the concentration of the atomic gold trough the following equation (Eq.2):

$$[\boldsymbol{AuNRs}] = \frac{[Au]}{V_{AuNR} * \frac{\rho_{gold}}{AW_{gold}} * N_A} = \frac{[Au]}{\left(\frac{1}{4}\pi w^2(l-w) + \frac{1}{6}\pi w^3\right) * \frac{\rho_{gold}}{AW_{gold}} * N_A} \qquad (\boldsymbol{Eq.S2})$$

AW_{gold} indicates the atomic weight of gold (196.97 g mol^{-1}) and N_A is the Avogadro number.

- **AuNTs**

The shape of each AuNTs was treated as a triangular nanoprism (Fig. S1b). The volume can be calculated by the following formula:

$$\boldsymbol{V_{AuNTs}} = A_b * t_{prism} = \frac{l * h}{2} * t \qquad (\boldsymbol{Eq.S3})$$

in which A_b is the triangle base area, with l and h corresponding to the edge length and the height of the equilateral triangle (evaluated from TEM analysis, see Table S1), and t being the nanoprism thickness.[8] AuNTs concentration can be derived from the concentration of the atomic gold trough the following equation:

$$[\boldsymbol{AuNTs}] = \frac{[Au]}{V_{AuNT}\ \frac{\rho_{gold}}{AW_{gold}}\ N_A} = \frac{[Au]}{\frac{l * h}{2} * t\ \frac{\rho_{gold}}{AW_{gold}}\ N_A} \qquad (\boldsymbol{Eq.S4})$$

AW_{gold} indicates the atomic weight of gold (196.97 g mol^{-1}) and N_A is the Avogadro number.

S2.6 | N_3-AuNRs and N_3-AuNTs

N_3-AuNRs and N_3-AuNTs were prepared by mixing citrate-AuNRs and citrate-AuNTs with a mixture containing an excess of ligand molecules, LA and LA@N_3, with respect to citrate anions (the excess was evaluated with respect to the theoretical moles of ligand which can cover the AuNMs surface). The theoretical number of ligand molecules necessary to cover the surface of each AuNR can be estimated through geometrical considerations and considering the following approximations: i) the colloidal solution of citrate-AuNRs contains only nanorods with average size (length and width) evaluated by TEM analysis; ii) the nanorods possess a cylindrical body with two hemispherical caps. Similarly, in the case of AuNTs, it can be considered that the colloidal solution of citrate-AuNTs contains only regular triangular gold nanoprisms, with an average edge length and height evaluated by TEM analysis, and thickness determined as reported in literature.[8] Assuming that the footprint size, *i.e.* the average areas occupied by the ligand molecules on the AuNMs surface, for LA and LA@N_3 is 0.25 nm^2,[13] the theoretical moles of ligand molecules necessary to cover the surface of all nanorods/nanoprisms in the colloid solution is given by eq. S5.

$$\mathbf{n_{lig}} = \frac{\left(\frac{(\mathrm{A_{tot}})_{\mathrm{AuNMs}}}{0.25\mathrm{nm}^2}\right)}{\mathrm{N_A}} \qquad (\boldsymbol{Eq.S5})$$

In a typical procedure, citrate-stabilized AuNMs are basified until pH 9 by adding NaOH 1 M and, in a separate vial, the mixture of heterobifunctional ligands LA and LA@N_3 is prepared (NaOH solution pH 9). To afford N_3-AuNRs, citrate-AuNRs (10.0 mL) were mixed with a 9:1 ratio of ligands (1.4 mL mixture containing $6.5 \cdot 10^{-6}$ mol of LA and $7.3 \cdot 10^{-7}$ mol of LA@N_3). Likewise, N_3-AuNTs were obtained by mixing citrate-AuNTs (6.5 mL) with a 9:1 ratio of ligands (2.6 mL mixture of $1.3 \cdot 10^{-5}$ mol of LA and $1.5 \cdot 10^{-6}$ mol, of LA@N_3). To allow ligand exchange, both N_3-AuNMs were kept under stirring in the dark for 16 h at room temperature, and the citrate displacement was verified by UV-Vis-NIR spectroscopy. Finally, ligand excess was removed through two centrifugation cycles (15 min, 7000 rpm, 4 °C); after each cycle, the precipitated azide-labeled AuNMs were resuspended in a fresh solution of NaOH solution (pH 9), to ensure the stability of the colloid. As prepared, N_3-AuNRs/AuNTs were stored in the dark at 4 °C until further use.

S2.7 | FeMC6*a-$(PEG)_4$@AuNRs and FeMC6*a-$(PEG)_4$@AuNTs

The conjugation of FeMC6*a-$(PEG)_4$-DBCO to N_3-exposing AuNRs and AuNTs was carried out by means of the SPAAC reaction, as already reported by us.[14] N_3-AuNRs (7.0 mL, pH 9) and N_3-AuNTs (6.0 mL, pH 9) were incubated with the clickable FeMC6*a-$(PEG)_4$-DBCO (65.0 µL of a stock solution $2.14 \cdot 10^{-3}$ M in DMF for AuNRs and 3.65 µL of a stock solution $1.23 \cdot 10^{-3}$ M in DMF for AuNTs) for 4 h at room temperature in the dark. The course of the click reaction was ascertained through UV-Vis-NIR spectroscopy. The excess of the unbound FeMC6*a-$(PEG)_4$-DBCO was removed through four cycles of centrifugation and resuspension (6500 rpm, 30 min, 4 °C). After each cycle, the supernatant containing the unbound enzyme was discarded and the pellet, containing the nanomaterials, was redispersed in an equal volume of an aqueous solution of NaOH (pH 9), to safeguard the stability of the colloidal solution. As already performed by us, after the first cycle, the pellet was resuspended in an aqueous solution of NaOH pH 9 with 50% (v/v) TFE, to get rid of the enzyme excess which could be non-specifically adsorbed on AuNMs surface.[15] The prepared nanoconjugates were promptly used for subsequent experiments.

S3 | Characterization of the nanosamples and nanoconjugates

S3.1 | Vis-NIR spectroscopy and TEM for CTAB-capped AuNMs

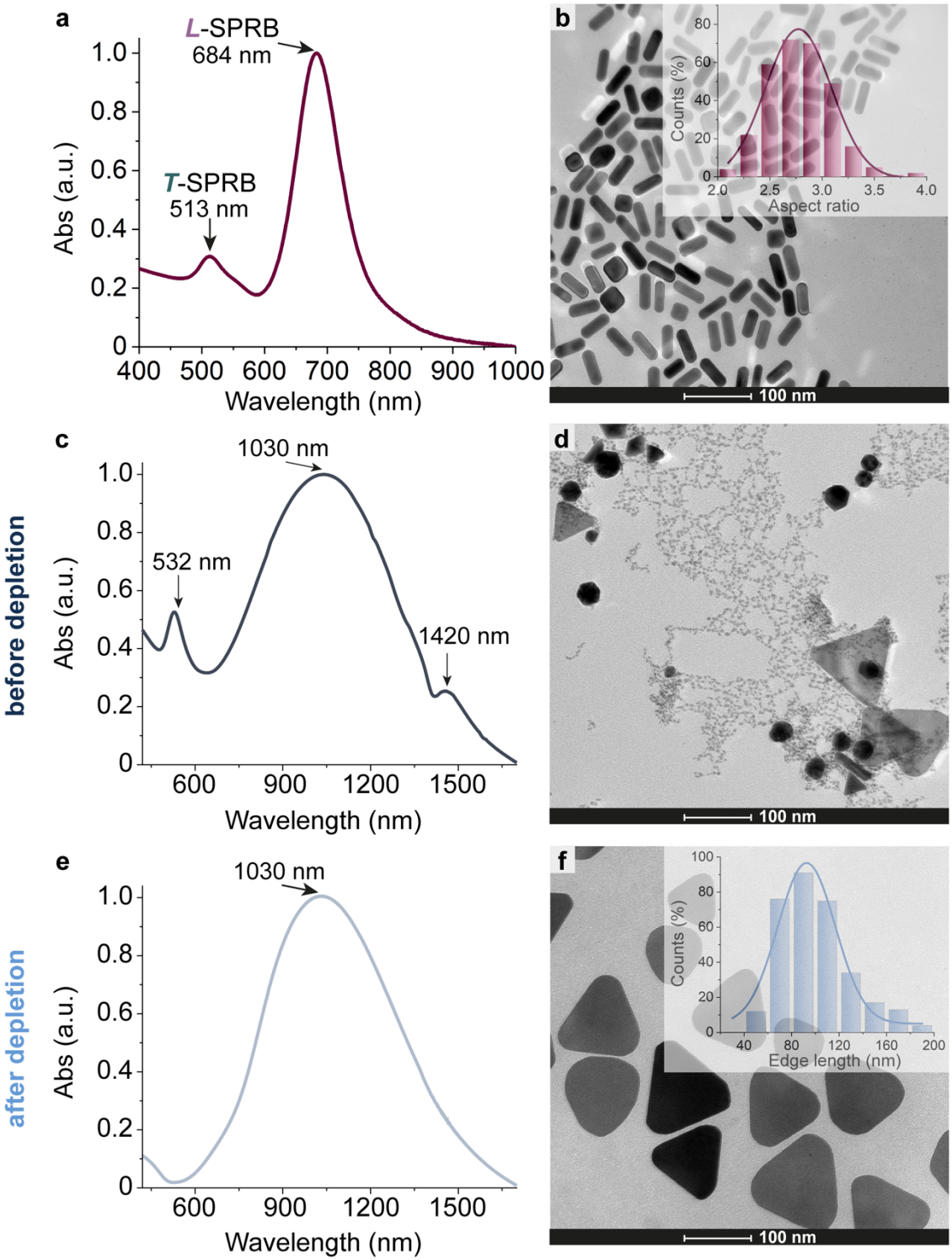

Figure S2. a) Vis-NIR spectrum of CTAB-AuNRs, along with the corresponding b) TEM micrograph. *Inset.* Histogram of the aspect ratio (AR) distribution and Gaussian fit. Vis-NIR spectra of AuNTs, c) before and e) after the micelle-induced depletion procedure. TEM micrographs of AuNTs d) before and f) after the depletion. *Inset.* Histogram of the edge length distribution (in nm) and Gaussian fit.

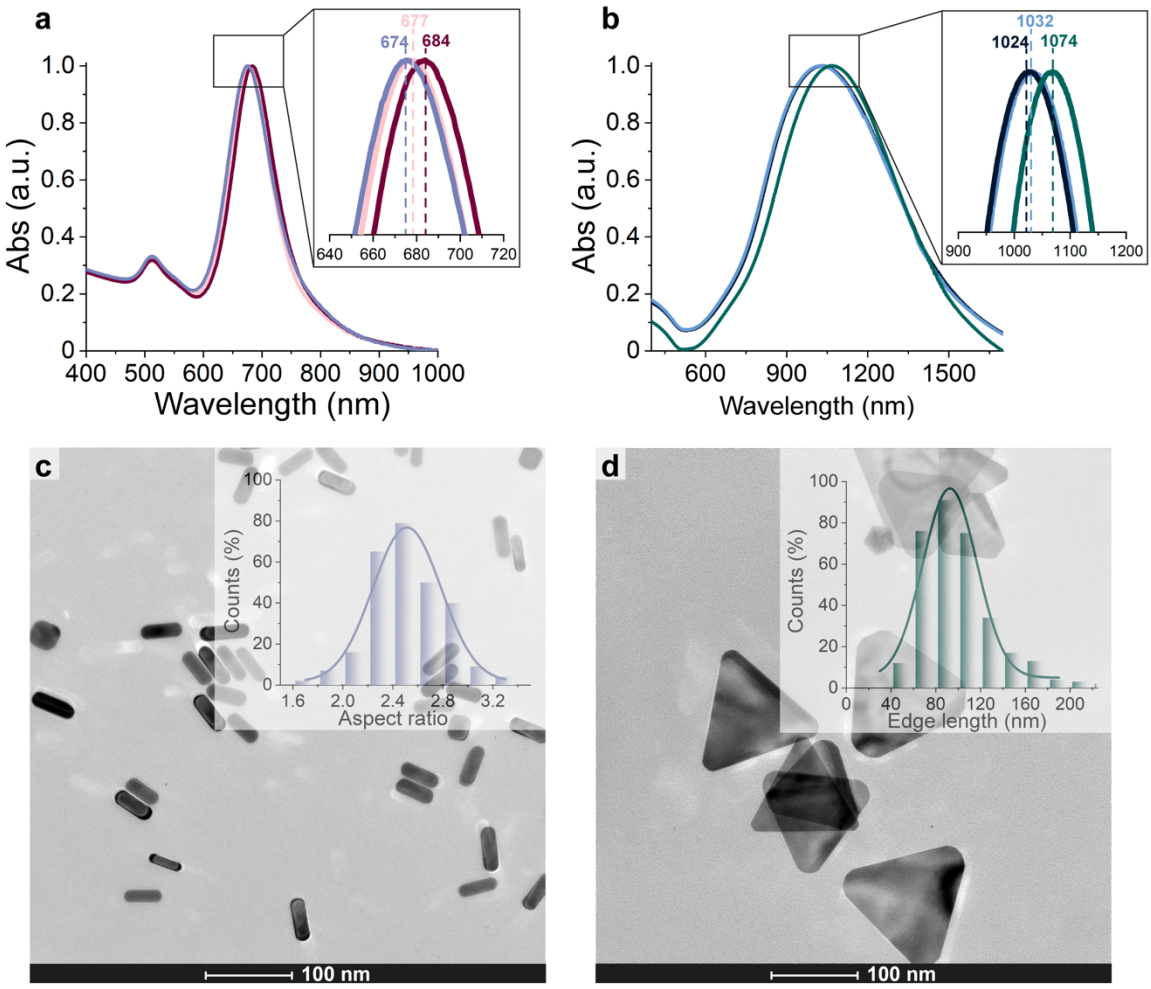

Figure S3. From CTAB- to citrate-AuNRs and AuNTs. a) Superimposition of the normalized Vis-NIR spectra of CTAB-AuNRs (dark red line), PSS-AuNRs (light pink line) and citrate-AuNRs (light violet line). b) Superimposition of the normalized Vis-NIR spectra of CTAB-AuNTs (light blue line), PSS-AuNTs (dark blue line) and citrate-AuNTs (turquoise line). c) TEM micrograph of citrate-AuNRs and *inset* histogram of the aspect ratio distribution and Gaussian fit. d) TEM micrograph of citrate-AuNTs and *inset* histogram of the edge length (in nm) distribution and Gaussian fit.

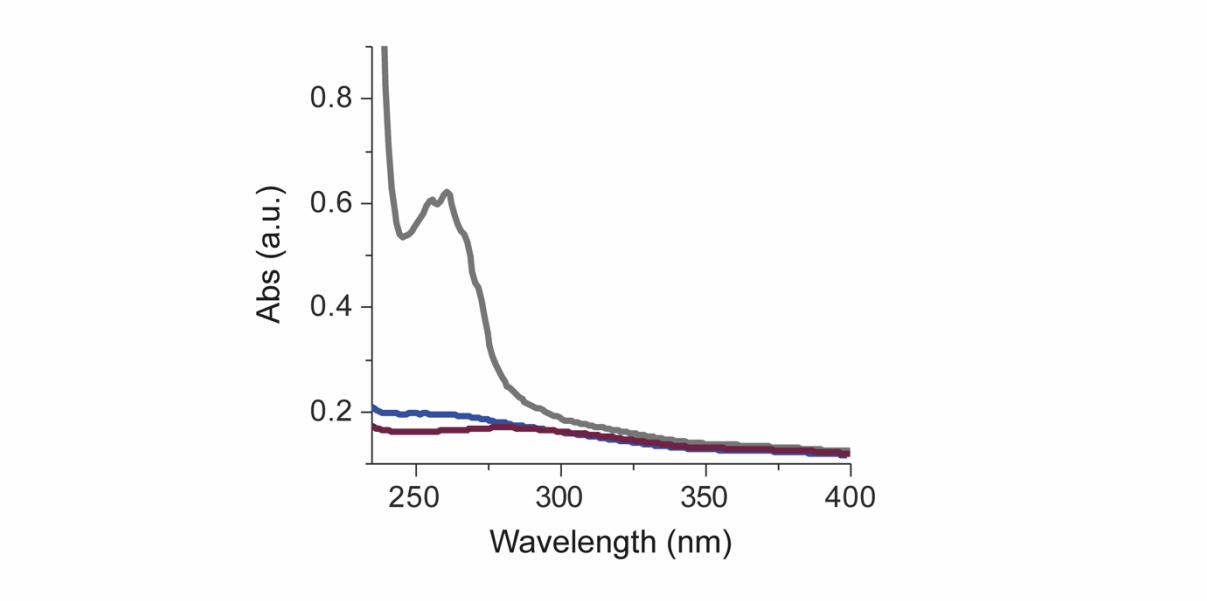

Fig. S4. Superimposition of the UV spectra of PSS-AuNRs (gray line), citrate-AuNRs (blue line) and citrate-AuNTs (dark red line). The lack in the citrate-AuNMs spectra of the PSS absorption maxima is indicative of successful PSS to citrate exchange.

Na-PSS in aqueous solution displays two distinctive absorption bands in the UV region, around 196 and 226 nm, related to the π-π* transition of the substituted benzene ring. In the absence of CTAB, the polyanions (PSS^-) form hydrogen bonds with water molecules, some of which can be replaced by CTA^+ cations. As a consequence, the charge density on the benzene ring increases and the band gap of π-π^* transition decreases, and this leads to red-shifts of Na-PSS absorption maxima in PSS-AuNMs colloids, indeed they are positioned at 254 and 261 nm.[16]

Table S1. Mean values and standard deviations of the average dimensions evaluated for CTAB-AuNRs/AuNTs and citrate-AuNRs/AuNTs as obtained from TEM analysis.

Capping agent	**AuNRs**			**AuNTs**
	Length (l, in nm)	**Width** (w, in nm)	**AR** (l/w)	**Edge length** (nm)
CTAB	46 ± 4	16.9 ± 1.2	2.8 ± 0.3	92 ± 23
Citrate (stage 5)	48 ± 3	19 ± 3	2.5 ± 0.3	98 ± 24

S3.2 | XPS analyses

Details of the composition of the gold coating shell were obtained through X-ray photoelectron spectroscopy (XPS). In particular, signals corresponding to the binding energies (expressed in eV) of Au (4f), C (1s), N (1s), Br (3p and 3d at 66 eV), and O (1s) were observed in the low-resolution survey spectra of CTAB-AuNRs and CTAB-AuNTs (Fig. S5a, b).

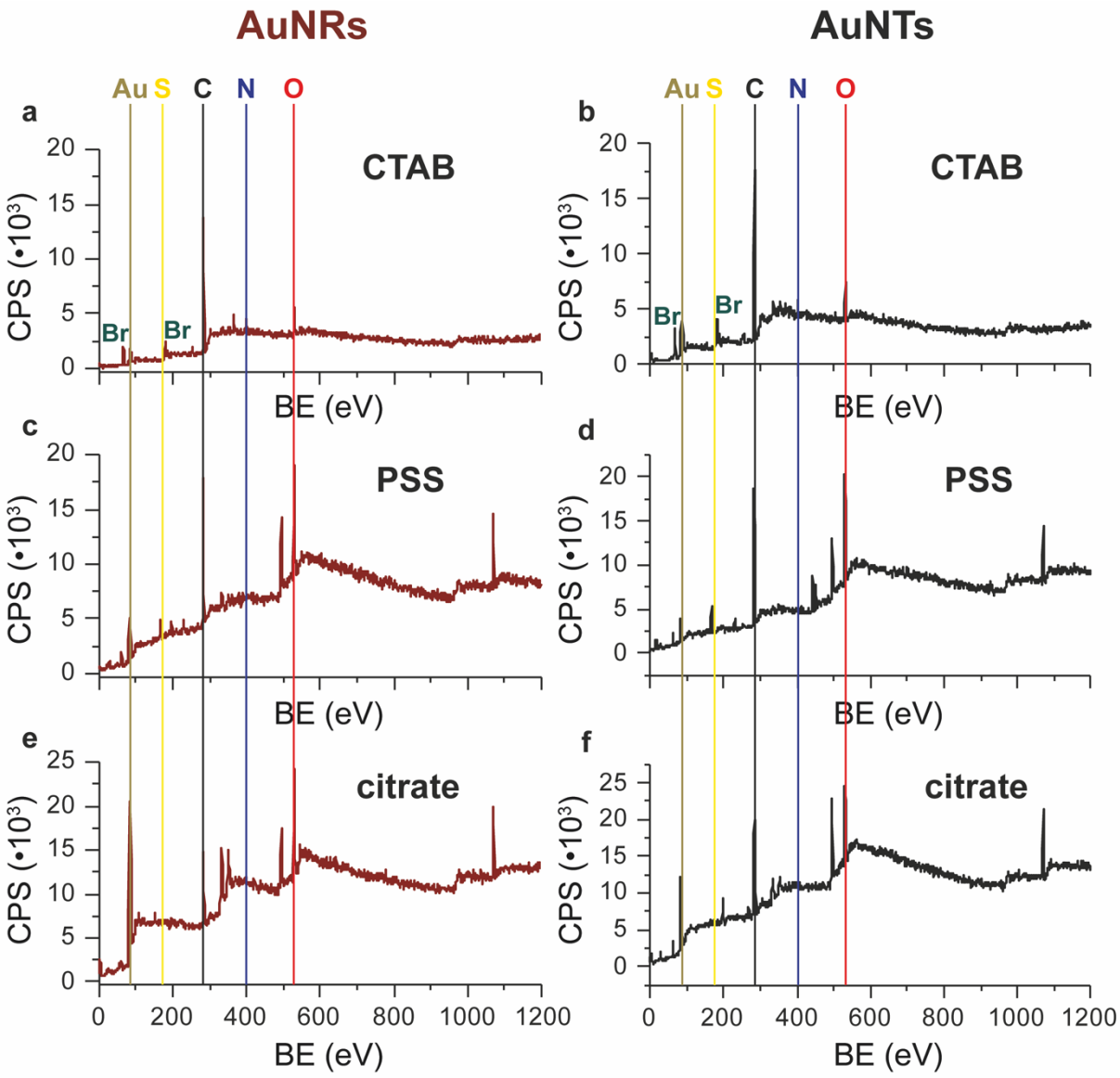

Fig. S5. XPS survey spectra of a) CTAB-AuNRs, c) PSS-AuNRs and e) citrate-AuNRs along with b) CTAB-AuNTs, d) PSS-AuNTs and f) citrate-AuNTs. BE stands for binding energy, while CPS for counts per second.

Furthermore, high-resolution spectra were acquired, specifically targeting the distinct spectral regions associated with gold and oxygen. Indeed, a typical Au 4f XPS spectrum features two contributions, corresponding to the Au $4f_{7/2}$ and Au $4f_{5/2}$ core-levels, due to spin-orbit coupling, as visible in Fig. S6. In bulk gold, these two peaks are separated by 3.67 eV, with the Au $4f_{7/2}$ peak at 84.0 eV and $4f_{5/2}$ at 87.67 eV. These values are consistent with the Au(0) oxidation state. In all the

nanosamples studied, appreciable deviations from the atomic or bulk standard gold values were not observed (Table S2). Noteworthy, the lack of any peak at BE of 85.8 eV and 89.1 eV, characteristic of the Au(III) oxidation state, indicate the absence of the gold precursor in the samples.[17] Concerning the high-resolution O 1s region, for all the nanosamples, the signal can be deconvoluted into three components (Fig. S6). In the case of CTAB-AuNRs and CTAB-AuNTs, these contributions have a BE of ~ 530, 531 and 532 eV for CTAB-AuNRs and CTAB-AuNTs (Fig. S6d and S6l respectively), and are indicative of the presence of some oxygen-containing molecules, such as water molecules trapped in the CTAB bilayer (near the tetramethylammonium heads)[18] or coming from the substrate holder (at ~ 532 eV), contribute which cannot be discarded.[19] For PSS-AuNRs and PSS-AuNTs (Fig. S6e and S6m), the low BE component at 531.9 eV and 531.7 eV (for PSS-AuNRs and PSS-AuNTs respectively) can be assigned to the SO_3^- moiety.[20] Finally, for citrate-AuNRs and citrate-AuNTs (Fig. S6f and S6n), the first two peaks at 531.6/531.5 eV and 532.8/533.0 eV are usually related to the O atoms involved in C-O and C=O bonds, whereas the signal having the higher BE, 535.8/535.7 eV, can be ascribed to O atoms of water molecules adsorbed in the layer.[18]

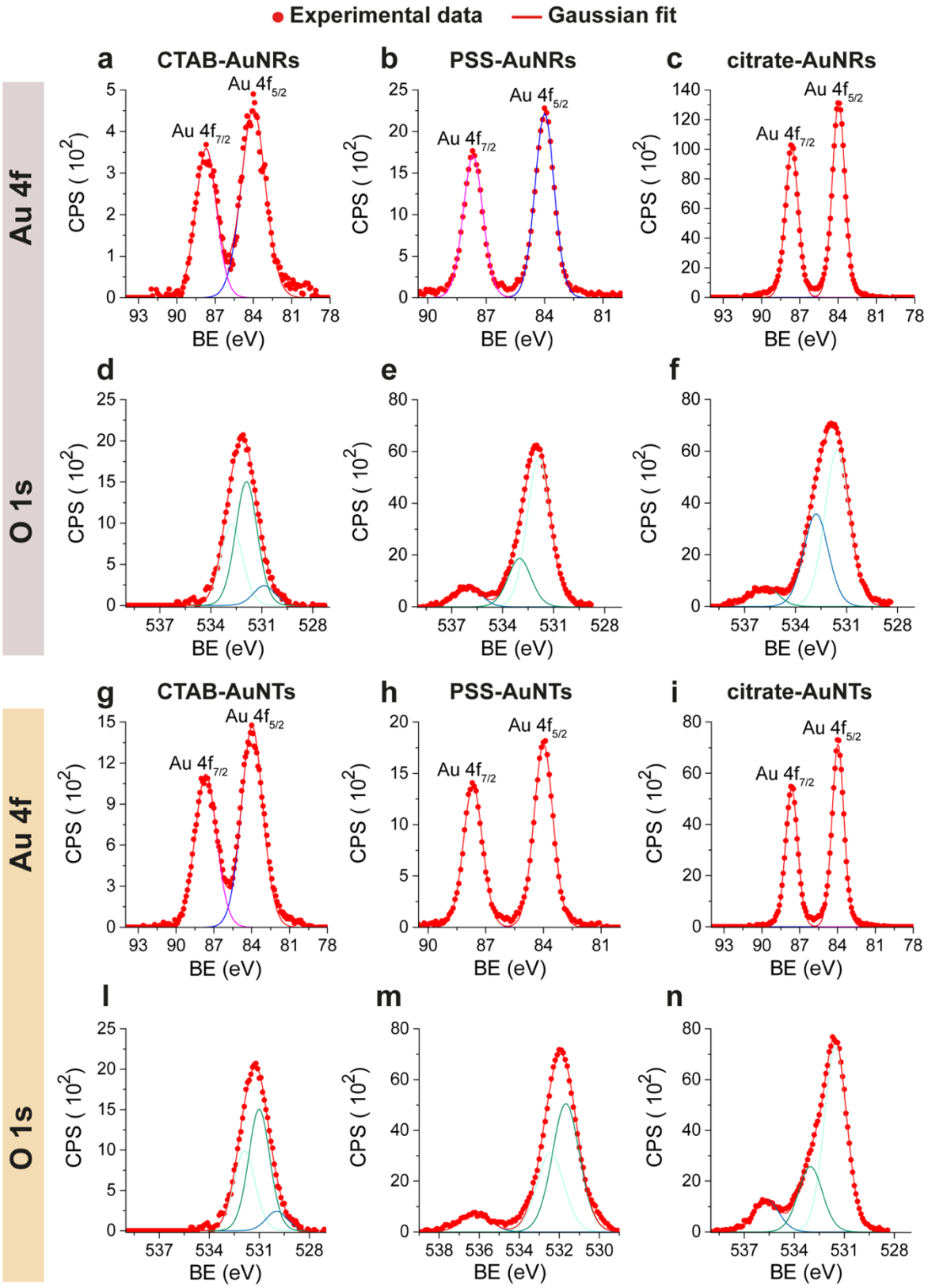

Fig. S6. XPS high-resolution spectra (count per second CPS vs binding energies BE in eV). For CTAB-AuNRs in the regions of a) Au 4f, d) O 1s; for PSS-AuNRs in the regions of B) Au 4f, E) O 1s; for citrate-AuNRs in the regions of C) Au 4f, F) O 1 s. For CTAB-AuNTs in the regions of G) Au 4f, L) O 1s; for PSS-AuNTs in the regions of H) Au 4f, M) O 1s; for citrate-AuNTs in the regions of I) Au 4f, N) O 1 s.

Table S2 lists the binding energy values for Au 4f in the six nanosamples under exam.

Table S2. Binding energy values (BE, in eV) determined from the high-resolution XPS spectra of CTAB-, PSS- and citrate-capped AuNRs and AuNTs.

Nanosamples	*Element*	*Assignation*	*BE (eV)*	*Fwhm*	*% area*
CTAB-AuNRs	**Au 4f**	Au $4f_{5/2}$	84.0	2.0	53.5
		Au $4f_{7/2}$	87.0	1.9	46.5
	Br 3p	Br $3p_{1/2}$	180.4	2.5	55.2
		Br $3p_{3/2}$	187.0	2.5	44.8
	C 1s	-C-C-/-C-H-	283.8	1.6	63.7
		-**C**-N$(CH_3)_3^+$	284.9	1.6	36.3
	N 1s	-C-**N**$(CH_3)_3^+$	401.3	1.9	100
	O 1s		530.0	1.5	12.9
			531.1	1.5	47.3
			532.3	1.5	39.8
CTAB-AuNTs	**Au 4f**	Au $4f_{5/2}$	84.0	2.0	50.5
		Au $4f_{7/2}$	87.6	2.0	49.5
	Br 3p	Br $3p_{1/2}$	180.2	2.5	55.2
		Br $3p_{3/2}$	186.9	2.5	44.8
	C 1s	-C-C-/-C-H-	283.8	1.5	74.8
		-**C**-N$(CH_3)_3^+$	285.0	1.5	25.2
	N 1s	C-**N**$(CH_3)_3^+$	401.1	1.7	100
	O 1s		530.0	1.5	9
			531.0	1.5	55
			531.9	1.5	36
PSS-AuNRs	**Au 4f**	Au $4f_{5/2}$	84.0	1.2	49.8
		Au $4f_{7/2}$	87.7	1.2	50.2
	S 2p	S $2p_{1/2}$	168.4	50.6	50.6
		S $2p_{3/2}$	169.6	49.4	49.4
	C 1s	-C-C-/-C-H-	285.1	1.5	91.3
			286.4	1.3	8.7
	O 1s		531.9	1.6	68.0
			533.0	1.6	22.0
			536.0	1.6	10.0
PSS-AuNTs	**Au 4f**	Au $4f_{5/2}$	84.0	1.2	50.1
		Au $4f_{7/2}$	87.7	1.2	49.9
	S 2p	S $2p_{1/2}$	168.3	1.5	51.6
		S $2p_{3/2}$	169.5	1.5	48.4
	C 1s	-C-C-/-C-H-	285.0	1.3	93.0
			286.1	1.5	7.0
	O 1s		531.7	1.6	56.3
			532.4	1.6	34.7
			536.1	1.6	8.9

Citrate-AuNRs	**Au 4f**	Au $4f_{5/2}$	84	1.2	49.6
		Au $4f_{7/2}$	87.6	1.2	50.4
	C 1s	-C-C-/- **C**-H-	285.2	1.5	74.5
		-**C**-O-R-	286.8	1.5	12.6
		-**C**(=O)-O-	288.6	1.5	12.7
	O 1s		531.6	1.7	58
			532.8	1.7	34.4
			535.8	1.7	7.6
Citrate-AuNTs	**Au 4f**	Au $4f_{5/2}$	84	1.1	50.0
		Au $4f_{7/2}$	87.6	1.1	50.0
	C 1s	-C-C-/- **C**-H-	285.2	1.5	71.8
		-**C**-O-R-	286.6	1.5	11.9
		-**C**(=O)-O-	288.5	1.5	16.4
	O 1s		531.5	1.6	63.8
			533.0	1.7	24.1
			535.7	1.7	12.1

Table S3. ζ-potential values and standard deviations were evaluated after each surface manipulation of the target gold nanomaterials.

	ζ-potential value (mV)	
Capping agent	**AuNRs**	**AuNTs**
Thiosulfate	/	-33.3 ± 0.7
CTAB	+48 ± 2	+47.6 ± 0.8
PSS (stage 3)	-34.7 ± 0.5	-35 ± 2
Citrate (stage 5)	-45.6 ± 1.2	-47.1 ± 0.4

S3.3 | FT-IR spectroscopy

The replacement of CTAB with PSS molecules was confirmed by the disappearance of the C-N stretching bands at ≈ 960, 940 and 910 cm^{-1} (Fig. S7a for AuNRs and Fig. S7e for AuNTs), and the appearance of PSS characteristic bands at ≈ 1180, 1120, 1040 and 1008 cm^{-1}, typical of $R\text{-}SO^{3-}$ groups (Fig. S7b for AuNRs and Fig. S7f for AuNTs).[21,20] The replacement of PSS by citrate ions was supported by the presence of a peculiar band at ≈ 1580 cm^{-1}, due to the stretching of carboxylate moieties.[10] Further, as CTAB molecules show intense bands associated with sp^3 C−H stretching (2900-2800 cm^{-1}, values of well-organized methylene chains in self-assembled monolayers)[22] and $-CH_3$ deformation (1480-1450 cm^{-1}), attenuation of these bands in the final citrate samples is an additional proof of CTAB replacement (Fig. S7c for AuNRs and Fig. S7g for AuNTs). Regarding the IR signals coming from the ligand molecules for the pelleted N_3-AuNMs,[23–25] the bands at ≈ 2920 and 2850 cm^{-1} are related to asymmetric and symmetric vibrations, respectively, of the methylene groups. Further, the bands at ≈ 1690 and 1540 cm^{-1} are mainly associated with the C=O and CO_2^- stretching vibrations of lipoic acid. Important to notice is the prominent band ≈ 1650 cm^{-1}, which can be assigned to the stretching of the C=O involved in the secondary amide bond, as well as the signal at 2100 cm^{-1}, which can be ascribed to the stretching of the azide moieties.[26] The presence of this latter signal supports the success of the ligand exchange reaction (Fig. S7d for AuNRs and Fig. S7h for AuNTs).

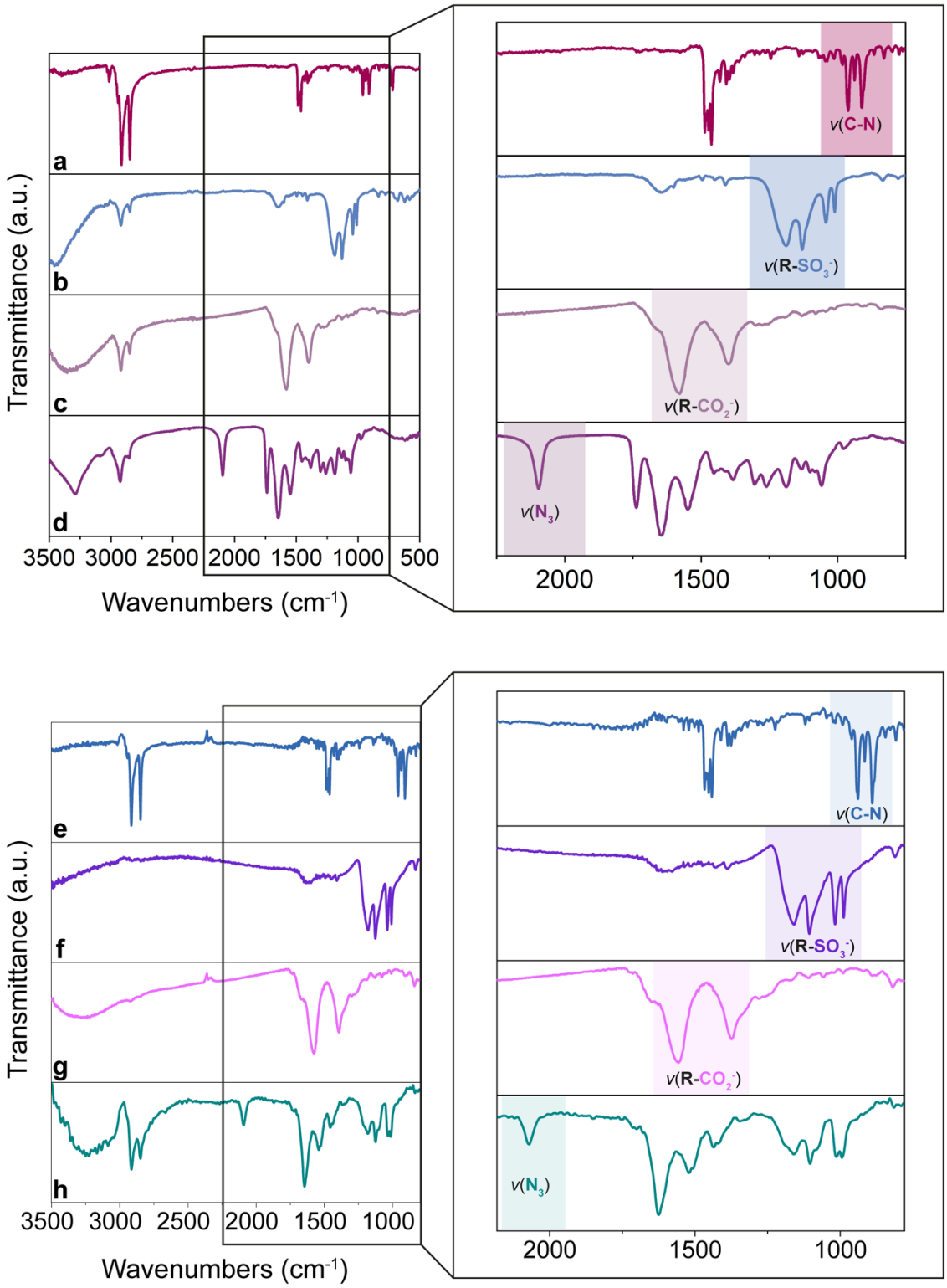

Fig. S7. Comparison of ATR FT-IR spectra gathered for both AuNMs. In particular, a) CTAB-AuNRs, b) PSS-AuNRs, c) citrate-AuNRs and d) N_3-AuNRs and e) CTAB-AuNTs, f) PSS-AuNTs, g) citrate-AuNTs and h) N_3-AuNTs along with a zoom of the fingerprint region, to highlight the peculiar signals from the coating molecules.

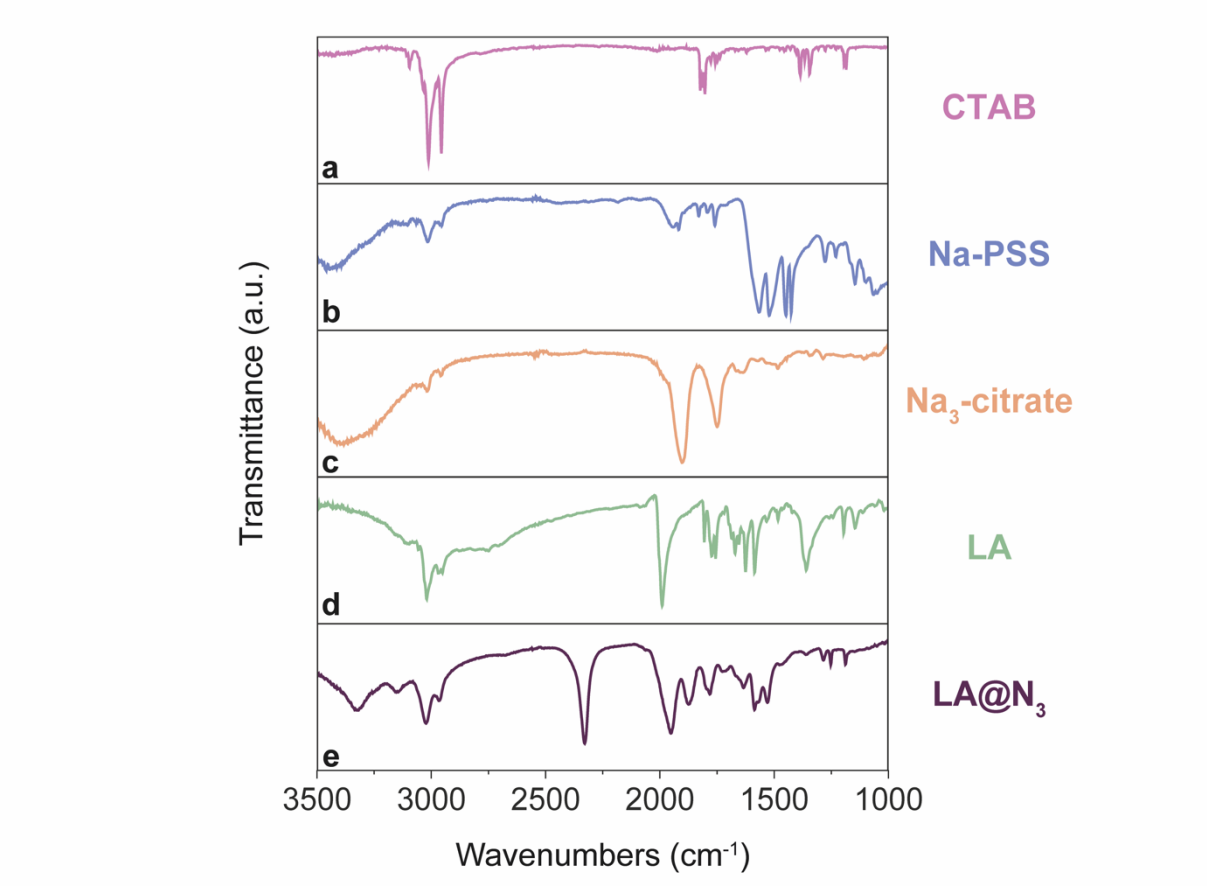

Fig. S8. Superimposition of ATR FT-IR spectra for commercially available CTAB (red line), Na-PSS (M_w 70 kDa) (blue line), Na_3-citrate (brown line), LA (orange line) and the synthesized LA@N_3 (green line).

S3.4 | Heme content in the nanoconjugate-containing samples

The concentration of FeMC6*a in the nanoconjugate samples was estimated by quantifying the heme content, following the method reported by Onoda et al.[27] In this protocol, treatment of AuNMs with potassium cyanide causes decomposition of the gold nanomaterial, thus quenching the SPRB, and yields the bis-cyanide complex of the heme-containing catalyst, characterized by an absorption band at 416 nm. Using the molar extinction coefficient at this wavelength (ε^{416} = 61754 M^{-1} cm^{-1}), it was possible to estimate the enzyme concentration from the UV-Vis spectra. Stock solutions of KCN 1 M were prepared in Milli-Q water and stored at 4 °C. All the etching reactions were started in a fume-hood by pipetting the according volumes of the aqueous solution of KCN into a plastic cuvette containing the samples. In details, aliquots of the samples (800 µL) were subjected to centrifugation (10500 rpm, 15 min, 4° C), to obtain a concentrated pellet (10 µL). Then, the aqueous solution of KCN (190 µL, $2.5 \cdot 10^{-2}$ M) was added to the pellet and the mixture was kept in incubation for 20 min. AuNMs decomposition was ascertained by following the disappearance of the typical plasmonic bands and the appearance of the band at 416 nm, related to the formation of the FeMC6*a bis-cyanide complex (Fig. S9). By using this method, the concentrations of FeMC6*a in FeMC6*a-$(PEG)_4$@AuNRs and FeMC6*a-$(PEG)_4$@AuNTs were found to be $7.2 \cdot 10^{-7}$ M and $6.8 \cdot 10^{-7}$ M, respectively.

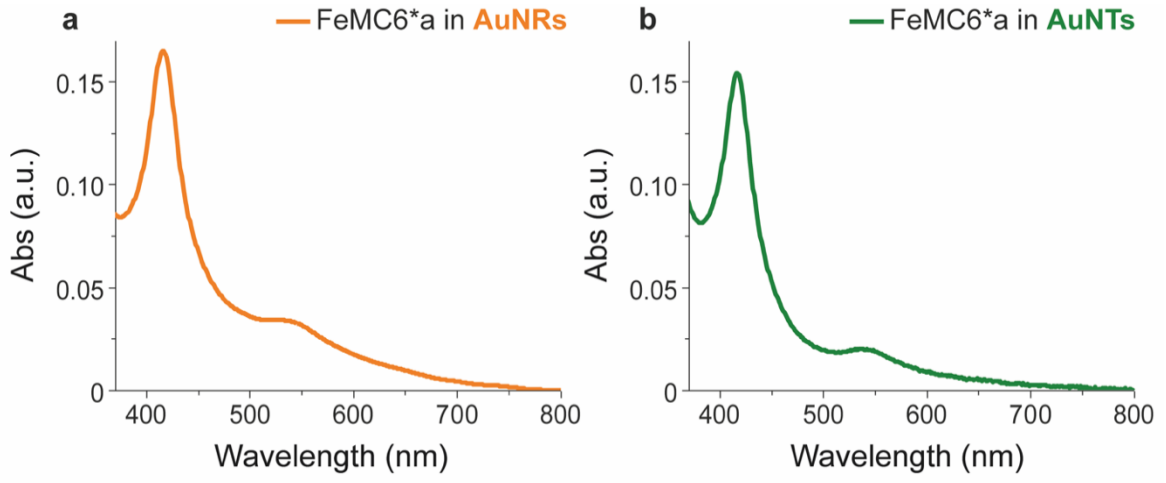

Fig. S9. Vis spectrum of the bis-cyanide complex obtained from a) FeMC6*a-$(PEG)_4$@AuNRs and b) FeMC6*a-$(PEG)_4$@AuNTs.

S3.5 | Evaluation of number of FeMC6*a coating AuNRs and AuNTs

The experimental loading of FeMC6*a on AuNRs and AuNTs was evaluated by estimating the gold concentration with ICP-MS and the iron concentration by the cyanide method. The results are reported in Table S4.

Table S4. Evaluation of the experimental average loading of FeMC6*a around AuNRs and AuNTs for the prepared nanoconjugates.

	[Au] (10^{-4} **M)**	**[Fe]** (10^{-6} **M)**	**[AuNMs]** (10^{-9} **M)**	**Fe/AuNM**
FeMC6*a-$(PEG)_4$@AuNRs	2.20	0.72	0.38	1900
FeMC6*a-$(PEG)_4$@AuNTs	1.15	0.68	0.049	13877

S3.6 | CD studies

The samples for CD analysis were prepared in buffer phosphate 10 mM pH 6.5 with 50% (*v/v*) TFE, to a final enzyme concentration of $3.5 \cdot 10^{7}$ M. The spectra were acquired using quartz cuvettes with 1 cm path lengths. Mean residue ellipticities [θ] were calculated using the following equation:

$$[\theta] = \frac{\theta_{obs}}{10 \cdot l \cdot C \cdot n} \qquad \textbf{(Eq. S6)}$$

in which θ_{obs} is the ellipticity measured in millidegrees, l is the path length of the cell in centimeters, C is the concentration in moles per liter, and n is the number of residues for the immobilized enzyme (25 residues).

S3.7 | Catalytic assays

All catalytic assays were carried out at 25 °C and under magnetic stirring, using quartz cuvettes with 1 cm path lengths. The experiments were performed by following the increase in absorbance of the $ABTS^{\bullet+}$ radical cation, obtained by the enzyme catalyzed oxidation of ABTS in presence of hydrogen peroxide.[28] The reaction course was followed for 5 min, after the addition of the oxidant at 0.5 min. The collected kinetic curves were employed to extract the reaction initial rates (v_0). ABTS and H_2O_2 stock solutions were freshly prepared in Milli-Q water, and their initial concentration was determined by UV-Vis spectroscopy (ABTS, $\varepsilon^{340} = 36600\ M^{-1}\ cm^{-1}$, H_2O_2, $\varepsilon^{240} = 39.4\ M^{-1}\ cm^{-1}$). Kinetic parameters were determined by varying H_2O_2 concentration at fixed ABTS concentrations and vice versa. All reactions were carried out in phosphate buffer (50 mM, pH 6.5), in the presence of TFE (50% *v/v*). In the experiments performed at variable H_2O_2 concentration (in the range 0.1-250 mM), the ABTS concentration was kept constant at 5.0 mM, while the experiments at variable ABTS concentration (in the range 0.1-5.0 mM) were carried out using H_2O_2 100 mM. All the kinetic curved were acquired in triplicate. The initial rates were converted from Abs^{660}/min to mM/s ($ABTS^{\bullet+}$ $\varepsilon^{660} = 1.44 \cdot 10^4\ M^{-1}\ cm^{-1}$) and the experimental data were fitted with a two-substrate Michaelis-Menten equation.[29] The analysis of the experimental kinetic data by Michaelis-Menten fitting provided directly k_{cat} and K_m for H_2O_2 and ABTS, from which the catalytic efficiencies (k_{cat}/K_m) are derived.

S4 | References

1 N. R. Jana, L. Gearheart and C. J. Murphy, *Adv. Mater.*, 2001, **13**, 1389–1393.
2 C. J. Murphy, T. K. Sau, A. M. Gole, C. J. Orendorff, J. Gao, L. Gou, S. E. Hunyadi and T. Li, *J. Phys. Chem. B*, 2005, **109**, 13857–13870.
3 C. J. Murphy, L. B. Thompson, D. J. Chernak, J. A. Yang, S. T. Sivapalan, S. P. Boulos, J. Huang, A. M. Alkilany and P. N. Sisco, *Current Opinion in Colloid & Interface Science*, 2011, **16**, 128–134.
4 B. Nikoobakht and M. A. El-Sayed, *Chem. Mater.*, 2003, **15**, 1957–1962.
5 L. Scarabelli, M. Grzelczak and L. M. Liz-Marzán, *Chem. Mater.*, 2013, **25**, 4232–4238.
6 L. Scarabelli, A. Sánchez-Iglesias, J. Pérez-Juste and L. M. Liz-Marzán, *J. Phys. Chem. Lett.*, 2015, **6**, 4270–4279.
7 R. del Caño, J. M. Gisbert-González, J. González-Rodríguez, G. Sánchez-Obrero, R. Madueño, M. Blázquez and T. Pineda, *Nanoscale*, 2020, **12**, 658–668.
8 B. Pelaz, V. Grazu, A. Ibarra, C. Magen, P. del Pino and J. M. de la Fuente, *Langmuir*, 2012, **28**, 8965–8970.
9 F. Zhang, J. Zhu, H.-Q. An, J.-J. Li and J.-W. Zhao, *J. Mater. Chem. C*, 2016, **4**, 568–580.
10 J. G. Mehtala, D. Y. Zemlyanov, J. P. Max, N. Kadasala, S. Zhao and A. Wei, *Langmuir*, 2014, **30**, 13727–13730.
11 G. Zambrano, M. Chino, E. Renzi, R. Di Girolamo, O. Maglio, V. Pavone, A. Lombardi and F. Nastri, *Biotechnology and Applied Biochemistry*, 2020, **67**, 549–562.
12 T.-S. Deng, J. E. S. van der Hoeven, A. O. Yalcin, H. W. Zandbergen, M. A. van Huis and A. van Blaaderen, *Chem. Mater.*, 2015, **27**, 7196–7203.
13 K. B. Sebby and E. Mansfield, *Anal Bioanal Chem*, 2015, **407**, 2913–2922.
14 G. Zambrano, M. Chino, E. Renzi, R. Di Girolamo, O. Maglio, V. Pavone, A. Lombardi and F. Nastri, *Biotechnology and Applied Biochemistry*, 2020, **67**, 549–562.
15 G. Zambrano, E. Ruggiero, A. Malafronte, M. Chino, O. Maglio, V. Pavone, F. Nastri and A. Lombardi, *IJMS*, 2018, **19**, 2896.
16 A. Mehrdad and E. Parvini, *J Solution Chem*, 2017, **46**, 908–930.
17 R. Nyholm, A. Berndtsson and N. Martensson, *J. Phys. C: Solid State Phys.*, 1980, **13**, L1091–L1096.
18 X.-P. He, X.-W. Wang, X.-P. Jin, H. Zhou, X.-X. Shi, G.-R. Chen and Y.-T. Long, *J. Am. Chem. Soc.*, 2011, **133**, 3649–3657.
19 E. Görlich, J. Haber, A. Stoch and J. Stoch, *Journal of Solid State Chemistry*, 1980, **33**, 121–124.
20 C. Falentin-Daudré, M. Aitouakli, J. S. Baumann, N. Bouchemal, V. Humblot, V. Migonney and J. Spadavecchia, *ACS Omega*, 2020, **5**, 8137–8145.
21 J. M. Chalmers and N. J. Everall, in *Polymer Characterisation*, eds. B. J. Hunt and M. I. James, Springer Netherlands, Dordrecht, 1993, pp. 69–114.
22 M. D. Porter, T. B. Bright, D. L. Allara and C. E. D. Chidsey, *J. Am. Chem. Soc.*, 1987, **109**, 3559–3568.
23 J. M. Abad, S. F. L. Mertens, M. Pita, V. M. Fernández and D. J. Schiffrin, *J. Am. Chem. Soc.*, 2005, **127**, 5689–5694.
24 J. Wang and Q. Xia, *Drug Delivery*, 2014, **21**, 328–341.
25 I. Turcu, I. Zarafu, M. Popa, M. Chifiriuc, C. Bleotu, D. Culita, C. Ghica and P. Ionita, *Nanomaterials*, 2017, **7**, 43.
26 M.-X. Zhang, B.-H. Huang, X.-Y. Sun and D.-W. Pang, *Langmuir*, 2010, **26**, 10171–10176.
27 A. Onoda, Y. Ueya, T. Sakamoto, T. Uematsu and T. Hayashi, *Chem. Commun.*, 2010, **46**, 9107–9109.
28 R. E. Childs and W. G. Bardsley, *Biochemical Journal*, 1975, **145**, 93–103.
29 K. A. Johnson, *FEBS Letters*, 2013, **587**, 2753–2766.